EES Batteries

Accepted Manuscript

This article can be cited before page numbers have been issued, to do this please use: S. Zhou, Z. Xu, C. Wang, C. Tang, J. Jian, M. Wang, H. Yao, H. Jin, Y. Lu and H. Ji, *EES Batteries*, 2026, DOI: 10.1039/D6EB00057F.

View Article Online
DOI: 10.1039/D6EB00057F

Broader context

Developing lithium-ion batteries for extreme temperatures (-40 to 60 °C) is critical for electric vehicles and space exploration. A key challenge lies in stabilizing the interfaces at both electrodes simultaneously under such conditions. We report a dual-salt electrolyte using $LiPO_2F_2$ and $LiPF_6$ in ethyl acetate/ethylene carbonate solvents. This design enriches $PO_2F_2^-$ anions around Li^+ ions, prompting their preferential decomposition to form robust, ion-conductive interphases rich in Li_3PO_4 and LiF. Consequently, 5 Ah graphite||NCM613 cells retain >80% capacity after 200 cycles at 60 °C and deliver 57% of room-temperature capacity at -40 °C, outperforming conventional electrolytes. This work provides a universal strategy for designing wide-temperature batteries through anion-mediated interfacial regulation.

View Article Online
DOI: 10.1039/D6EB00057F

ARTICLE

Weakly-Dissociated Lithium Salt Decouples Solvent-Anion Interfacial Dynamics for Wide-Temperature Lithium-Ion Batteries

Received 00th January 20xx,
Accepted 00th January 20xx

DOI: 10.1039/x0xx00000x

Shaoyun Zhou†[a,b], Zetai Xu†[a], Chaonan Wang†[a], Chao Tang[a,b], Junhua Jian[b], Meirong Wang[b], Hong-Bin Yao[a], Hongchang Jin*[a], Yuhao Lu*[b], Hengxing Ji*[a]

Developing lithium-ion batteries (LIBs) operable across extreme temperatures (−40 to 60°C) is imperative for electric vehicles and space technologies, yet hindered by incompatible interphasial requirements: cathode-electrolyte interphase (CEI) degradation at high temperatures and anode solid-electrolyte interphase (SEI) impedance surge at subzero conditions. Here, we report a novel dual-salt electrolyte composed of weakly-dissociated $LiPO_2F_2$ (LiDFP) and common-used $LiPF_6$ in an ethyl acetate (EA)/ethylene carbonate (EC) co-solvent, enabling wide-temperature LIB operation with exceptional interphasial stability. LiDFP with elevated solubility renders contact ion pairs and aggregates surrounding Li^+, enriching $PO_2F_2^-$ coordination within the Li^+ solvation shell. This unique solvation structure promotes the preferential decomposition of $PO_2F_2^-$ anions at electrode surfaces, forming thin, dense CEI/SEI layers dominated by Li_3PO_4 and LiF, which simultaneously enhance interphasial robustness and Li^+ transport. As a result, 5 Ah NCM613||graphite pouch cells deliver over 80% capacity retention after 200 cycles at 60°C and maintain 57% reversible capacity at −40°C. While the cell using $LiPF_6$-EC electrolyte retain 80% capacity after only 200 cycles at 45°C. By decoupling anion-mediated interfacial regulation from solvent-centric limitations, this work establishes a universal electrolyte paradigm to achieve intrinsically stable, wide-temperature LIBs.

Introduction

The development of lithium-ion batteries (LIBs) capable of stable operation across a wide temperature window remains a formidable challenge, primarily due to interphasial instabilities at both the cathode and anode.[1-5] At high temperatures (>45°C), both the cathode-electrolyte interphase (CEI) and anode solid-electrolyte interphase (SEI) become unstable. They undergo repeated dissolution/reformation, consuming cyclable Li^+. The CEI degradation accelerates transition metal (TM) dissolution from cathodes (e.g., NCM ternary material), which in turn facilitates the breakdown and subsequent rebuilding of CEI and SEI.[6,7] Such continuous rebuilds of CEI and SEI concurrently generate thick and resistive coatings at the cathode and anode surfaces, increasing impedance and reducing achievable battery capacity, particularly at low temperatures. It is noteworthy that the raised impedance at the anode side by SEI tends to result in lithium plating when charging the battery at low temperatures. Lithium plating is a primary cause of battery failure and safety hazards.[8-11] Thermally stable and Li^+ conductive CEI and SEI are essential to LIBs functioning in a wide temperature range, standing for the central importance in battery research.[12-14] As both CEI and SEI are the products of electrolyte decomposition, designing functional electrolytes that can generate thermally stable CEI under highly oxidative potential in the cathode and Li^+ conductive SEI under highly reductive potential in the anode becomes essential.

However, current electrolyte formulations struggle to balance these requirements, as thermally and electrochemically stable electrode-electrolyte interphases typically sacrifice interphasial Li^+ mobility. Furthermore, because electrolyte is in contact with both cathode and anode, almost no electrolyte design can form a stable CEI without compromising the SEI kinetics.[15-17] From an electrolyte perspective, the inherent limitations of widely used $LiPF_6$ in ethylene carbonate (EC)-based electrolytes further complicate interfacial control.[18,19] The strong dissociation of $LiPF_6$ in EC-dominated solvation structures results in solvent-rich coordination shells, favoring organic-rich CEI/SEI layers with excessive thickness and low Li^+ conductivity.[20-22] While cosolvents or additives (e.g., 1,1,2,2-tetrafluoroethyl-2,2,3,3-tetrafluoropropyl ether, fluoroethylene carbonate) can partially regulate solvation structures by enhancing anion participation, such approaches often prioritize either CEI's thermal stability or SEI's Li^+ conductivity. For instance, anion-coordinating additives like lithium bis (oxalate) borate (LiBOB) yield integrative and

[a] Hefei National Research Center for Physical Sciences at the Microscale, School of Chemistry and Materials Science, iChEM, University of Science and Technology of China; Hefei, Anhui 230026, China.
[b] Ningde Amperex Technology Limited (ATL), Key laboratory of consumer lithium-ion battery in Fujian, Ningde, 352100, China
† These authors contributed equally to this work.

View Article Online
DOI: 10.1039/D6EB00057F

ARTICLE

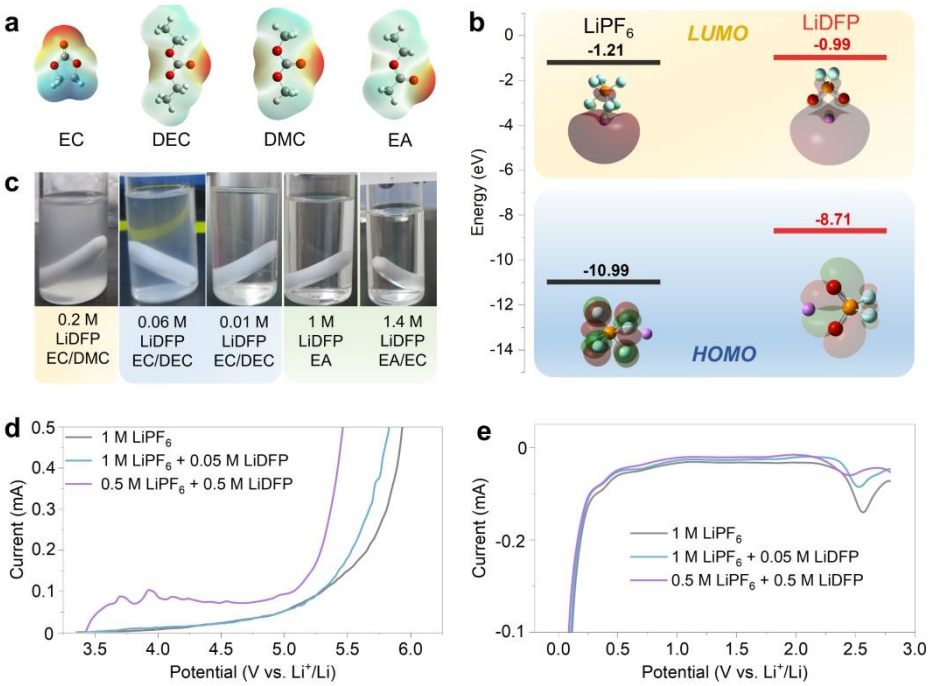

Figure 1. (a) Calculated electrostatic potential for EC, DEC, DMC and EA; (b) frontier molecular orbital (HOMO/LUMO) energy levels for $LiPF_6$ and LiDFP; (c) Visual comparison of electrolytes with varying LiDFP concentrations in EC-based (EC/DMC, EC/DEC) and EA-based (EA, EA/EC) solvent systems; (d) Anodic LSV profiles (3.0–6.0 V vs. Li^+/Li, 1 mV/s) and (e) Cathodic LSV profiles (3.0–0.01 V vs. Li^+/Li, 1 mV/s) of 1 M $LiPF_6$, 1 M $LiPF_6$ + 0.05 M LiDFP, and 0.5 M $LiPF_6$ + 0.5 M LiDFP in EA/EC (7:3 v/v) electrolyte

thermally stable CEI but increase SEI resistivity; whereas agents (e.g., vinylene carbonate) generate mechanically robust SEI with fragile CEI at high temperature. This trade-off underscores the need for lithium salts with high solubility but low dissociation degrees to decouple the solvation dynamics from interfacial reactions.[23-27]

Lithium difluorophosphate (LiDFP), a weakly-dissociated salt, presents a promising alternative. Its limited dissociation reduces solvent-dominated coordination, promoting anion-derived interphasial components (e.g., LiF, Li_3PO_4) that can enhance both CEI thermal stability and SEI ionic transport. However, LiDFP's low solubility in carbonate solvents (~0.1 M) limit its practical utility. Previous studies demonstrate that trace LiDFP additive improves interphasial properties, yet the low concentration fails to fully exploit its potential. Enhancing LiDFP solubility without compromising ionic conductivity or low-temperature fluidity could unlock its dual-functionality. This goal requires solvents that can both dissolve LiDFP at high concentrations and preserve broad liquidus ranges, a condition not satisfied by conventional carbonate solvents.

In this study, we report a weakly solvating electrolyte for wide-temperature LIBs by employing a dual-salt electrolyte, which contains weakly-dissociated LiDFP synergy with $LiPF_6$, coupled with a high-dielectric-constant ethyl acetate (EA)/ EC co-solvent. EA incorporation enhances LiDFP solubility in the carbonate-based solvents to 1.4 M while significantly decreasing electrolyte melting points. In the 0.5 M LiDFP/0.5 M $LiPF_6$ (EA/EC) electrolyte, LiDFP predominantly exists as contact ion pairs (CIPs) and aggregates (AGGs) substantially increasing $PO_2F_2^-$ anion coordination numbers in the primary solvation shells surrounding the Li+. This solvation structure allows $PO_2F_2^-$ anions preferentially decompose at electrode surfaces to form thin, dense, inorganic-rich (Li_3PO_4 and LiF) CEI/SEI that effectively enhance interphasial stability and kinetics. In 5 Ah pouch cells (NCM613||graphite), this electrolyte demonstrates exceptional thermal stability and low-temperature performance: >80% capacity retention after 200 cycles at 60°C; and 57% reversible capacity retention at -40°C, respectively. By strategically regulating lithium salt dissociation and solvation structures, this work provides an industrially viable electrolyte design strategy for developing wide-temperature LIBs.

Results and discussion

EA Co-solvent Enhances LiDFP Solubility for Improved Electrode Interfaces

LiDFP exhibits low solubility in common solvents such as EC, diethyl carbonate (DEC), and dimethyl carbonate (DMC), limiting its effectiveness in optimizing electrode interface structures. As lithium salt solubility typically correlates with solvent dielectric constant and

donor number (DN),[28,29] solvents with high dielectric constants and DN values were screened to enhance LiDFP solubility in carbonate-based electrolytes (Table S1). These included dimethyl sulfoxide (DMSO), triethyl phosphate (TEP), dimethoxyethane (DME), sulfolane (SL), and EA. LiDFP demonstrated high solubility (>9 wt.%) in all screened solvents.[30-33] However, DMSO, TEP, and SL exhibited excessive viscosity, while DME showed limited oxidative stability at the cathode. These solvents also present pronounced solvent co-intercalation risks with graphite anodes.[34-38] Consequently, EA emerges as a promising alternative to conventional carbonates due to its broad liquidus range (-83.6 to 77.1°C), low viscosity, and favorable electrochemical stability.[39] Plus, the

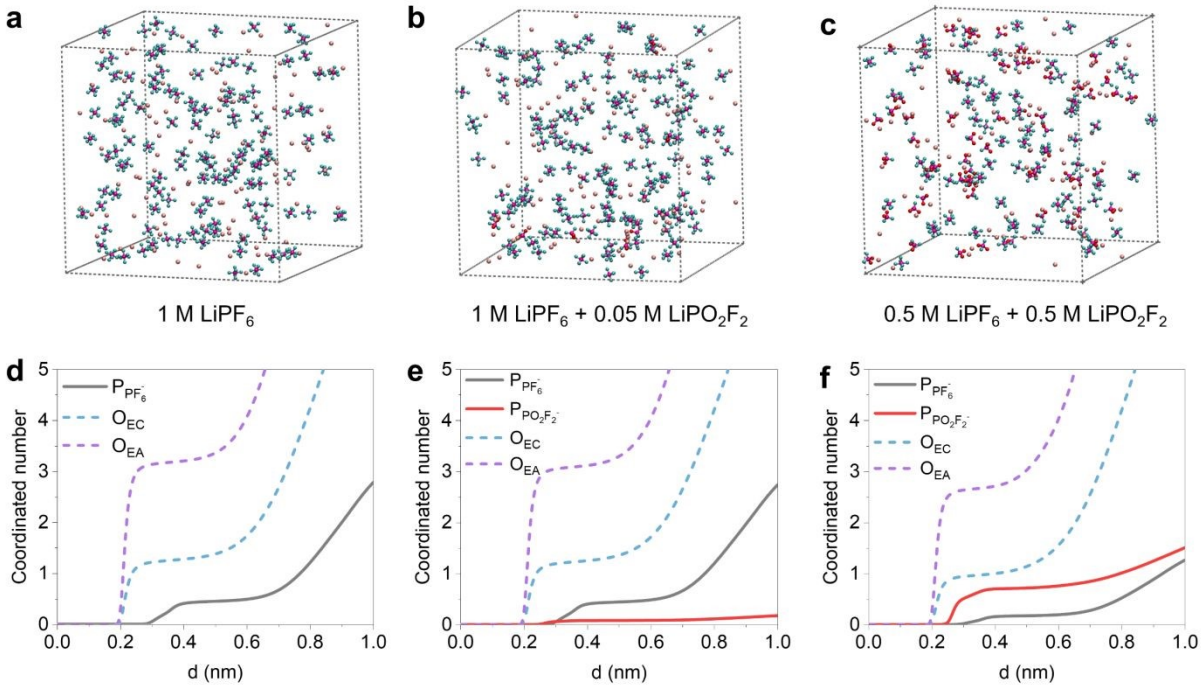

Figure 2. (a-c) Representative MD simulation snapshots depicting solvation structures in: (a) 1 M $LiPF_6$ EA/EC, (b) 1 M $LiPF_6$ + 0.05 M LiDFP EA/EC, and (c) 0.5 M $LiPF_6$ + 0.5 M LiDFP EA/EC. (d-f) Calculated Li^+ coordination number for: (d) 1 M $LiPF_6$ EA/EC, (e) 1 M $LiPF_6$ + 0.05 M LiDFP EA/EC, and (f) 0.5 M $LiPF_6$ + 0.5 M LiDFP EA/EC.

solubility of LiDFP in the EA co-solvent is increased to 1.4 M, around twenty times higher than in EC (<0.06 M, Figure 1c).

Surface electrostatic potential of EA relative to conventional solvents and electrochemical windows of LiDFP relative to $LiPF_6$ were investigated. Density functional theory (DFT) calculations indicate EA exhibits reduced cathodic electrostatic potential versus EC, reflecting weaker polarity and diminished Li+ solvation capability (Figure 1a).[40] Frontier molecular orbital analysis reveals LiDFP possesses a higher HOMO energy (-8.71 eV) than $LiPF_6$, signifying its preferential oxidative decomposition for CEI formation (Figure 1b). Linear sweep voltammetry (LSV) confirmed interfacial decomposition of LiDFP: 0.5 M LiDFP-EA/EC (7:3) electrolyte showed a distinct oxidation peak at ~3.5 V corresponding to CEI formation (Figure 1d).[41] Cathodic LSV profiles revealed suppressed EA reduction currents at ~2.5 V with increasing LiDFP content, indicating its critical role in anode passivation (Figure 1e).

Low LiDFP Dissociation Enables Anion-Rich Interfaces

Li^+ coordination in electrolytes was probed via Raman spectroscopy (Figure S1). In contrast to $LiPF_6$/EA that exhibited characteristic PF_6^- vibration (741 cm^{-1}), The Raman spectrum of LiDFP/EA presented concentration-dependent P-O bond signals. Critically, LiDFP caused negligible EA solvent peak shifts (848 cm^{-1} and 2940 cm^{-1}), contrasting with $LiPF_6$-induced peak broadening and wavenumber increases, indicating weaker Li^+-$PO_2F_2^-$ coordination versus Li^+-PF_6^- interactions. Beside, we included the binding energies with Li^+ for EC (−2.37 eV), ethyl methyl carbonate (EMC, −2.39 eV), DEC (−2.34 eV), DMC (−2.41 eV), EA (−2.20 eV), PF_6^-(−4.98 eV), and $PO_2F_2^-$(−5.68eV) (as shown in Figure S2). The binding energy between Li^+ and $PO_2F_2^-$ anions is higher than that with PF_6^-, and significantly higher than common solvents including EC and EA. Therefore, LiDFP acts as a weakly dissociating salt and disrupts the dominance of solvent coordination, resulting in a solvation structure in the electrolyte that is rich in CIPs and AGGs.[42] However, low dissociation typically compromises ionic conductivity. We measured the ionic conductivities and revealed fundamental differences between $LiPF_6$ and LiDFP in EA and EA/EC (7:3 v/v) systems (Table S2). Despite the high LiDFP solubilities in EA (1.1 M) and EA/EC (1.5 M), the electrolyte conductivities remained low (0.04 and 0.62 mS/cm, respectively). LiDFP addition substantially reduced conductivity even in $LiPF_6$-LiDFP dual-salt electrolytes, indicating limited dissociation of the salts. We thus investigated three types of salts, 1 M $LiPF_6$, 1 M $LiPF_6$ + 0.05 M LiDFP, and 0.5 M $LiPF_6$ + 0.5 M LiDFP, dissolved in EA/EC (7:3 v/v) to achieve a favorable electrolyte conductivity.

Molecular dynamics simulations elucidated Li^+ solvation structures. In dual-salt systems, increasing LiDFP content reduced Li^+ coordination with PF_6^-, EC, and EA while enhancing $PO_2F_2^-$ coordination. $PO_2F_2^-/PF_6^-$ and $PO_2F_2^-$/solvent ratios increased significantly with LiDFP/$LiPF_6$ ratios (Figure 2, Table S3). For single-salt systems, 1 M $LiPF_6$-EA showed Li^+ coordinated with 3.8 EA molecules and 0.8 PF_6^- anions, indicating predominant solvent-separated ion pairs (SSIPs) (Figure S3). Conversely, 1 M LiDFP-EA showed Li^+ coordinated with 2.5 EA molecules and 1.6 $PO_2F_2^-$ anions, with anion coordination >1 signifying increased CIPs and AGGs. This

anion-enriched structure promotes $PO_2F_2^-$ participation in interfacial reactions, suppressing solvent decomposition. Collectively, these results demonstrate that the preferential formation of phosphate-rich interphases inhibit parasitic reactions—highlighting LiDFP's functionality via low dissociation and anion-dominated solvation. To experimentally validate the anion coordination predicted by Molecular dynamics (MD) simulations, we performed Raman spectroscopy and deconvolution analysis on electrolytes with varying LiDFP content in Figures S4 and S5 (EA/EC co-colvent, 1 M $LiPF_6$ in EA/EC electrolyte, 1 M $LiPF_6$ + 0.05 M LiDFP in EA/EC electrolyte, and 0.5 M $LiPF_6$ + 0.5 M LiDFP in EA/EC electrolyte). The distribution confirms that LiDFP exists predominantly as CIPs and AGGs, markedly increasing the $PO_2F_2^-$ coordination number in the primary Li^+ solvation shell, in excellent agreement with the MD simulations.[43,44]

Battery tests evaluated LiDFP's impact on wide-temperature performance. 5 Ah NCM||Gr pouch cells employed mixed-salt electrolytes (Figure S6). High-temperature storage (60°C) showed cells with single-salt $LiPF_6$ electrolyte exhibited 9.7% expansion after 6 days and 17.2% after 24 days (Figure S7). LiDFP addition mitigated expansion: adding 0.05 M LiDFP showed 10.4% expansion after 24 days, while adding 0.5 M LiDFP showed only 3.8%, confirming enhanced high-temperature stability. At 25°C (Figure 3a), the 1 M $LiPF_6$ cell maintained 80% capacity after 407 cycles. The 1 M $LiPF_6$ + 0.05 M LiDFP extended this to 495 cycles. The 0.5 M $LiPF_6$ + 0.5 M LiDFP electrolyte exhibited superior stability, maintaining 80% capacity after 986 cycles (0.02% average decay/cycle). High-temperature cycling (45°C, Figure 3b) showed cells achieving 226,

LiDFP Enables Superior Wide-Temperature Cycling and Stability

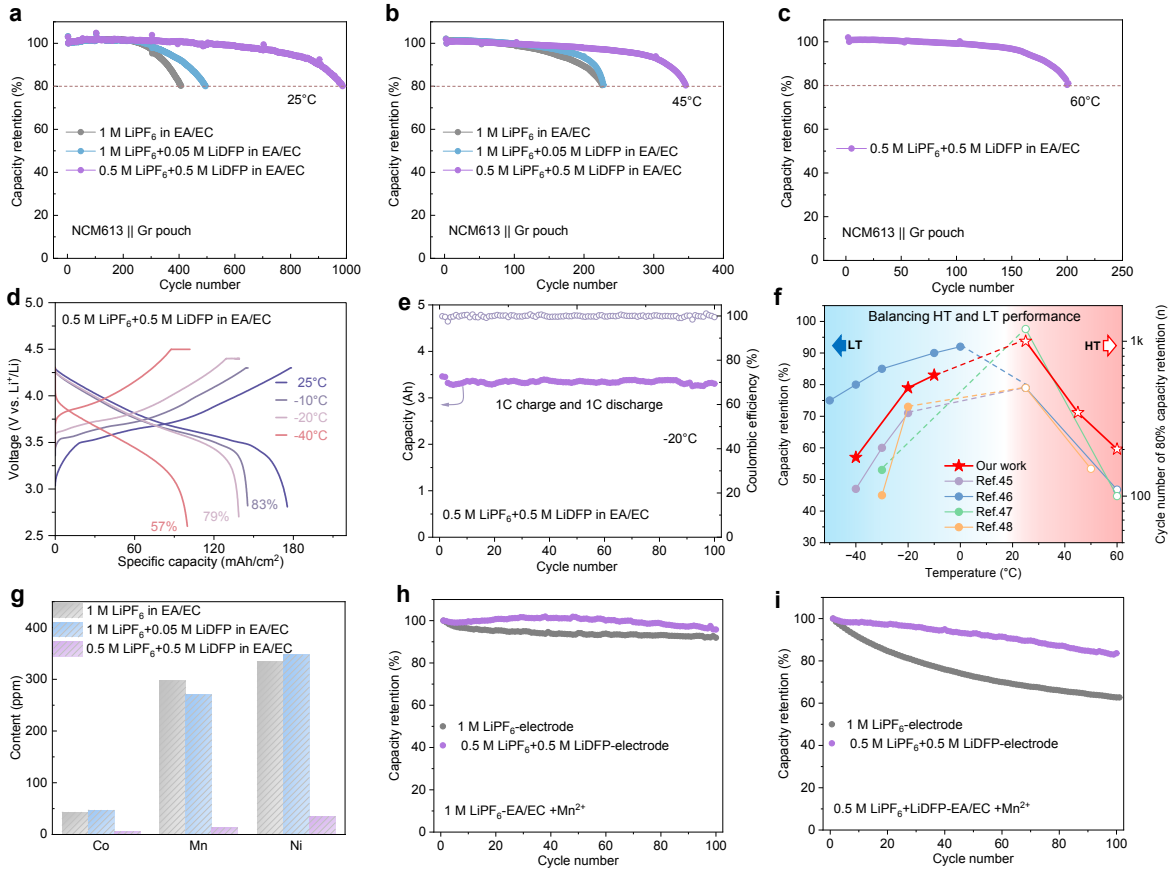

Figure 3. (a–c) Cycling performance of pouch cells at 25°C, 45°C, and 60°C, respectively. (d) Voltage profiles of pouch cells with 0.5 M $LiPF_6$ + 0.5 M LiDFP EA/EC at -40 to 25°C. (e) Low-temperature cycling performance in 0.5 M $LiPF_6$ + 0.5 M LiDFP EA/EC electrolyte (-20°C, 1C rate). (f) Benchmarking of the reported Gr-based full cells: cycle durability at high temperature and capacity retention at low temperature. (g) TM deposition concentrations on anodes after 280 cycles (25°C) quantified by ICP. (h, i) Cycling performance of cells reassembled with Mn^{2+} -added electrolytes: (h) LiPF6 baseline, (i) $LiPF_6$/LiDFP dual-salt system.

228, and 346 cycles to 80% retention, respectively. At 60°C, the 0.5 M $LiPF_6$ + 0.5 M LiDFP cell maintained 80% capacity after 200 cycles (Figure 3c). Thus, LiDFP significantly enhances both room- and high-temperature cycling. Rate performance (Figure S8) confirmed optimal performance for 0.5 M $LiPF_6$ + 0.5 M LiDFP at 0.3C to 4C, retaining 92.7% capacity at 4C. Low-temperature testing demonstrated 79% and 57% capacity retention at -20°C and -40°C, respectively, with negligible decay after 100 cycles at -20°C (Figure 3d and 3e). These results indicate $LiPF_6$/LiDFP dual-salt electrolyte achieves superior high/low-temperature performance balance versus literature (Figure 3f and Table S4).[45-48]

The dissolution of cathode TM ions induces detrimental crosstalk effects, compromising battery cycle life. To evaluate the suppression of TM dissolution by the LiDFP-derived interphase, we quantified TM deposition on the graphite anode surface via inductively coupled plasma (ICP) analysis. Cells cycled 280 times at 25°C exhibiting negligible capacity fade were disassembled prior to significant interphase degradation. Figure 3g depicts the TM content (Ni, Mn, Co) on the graphite anode. Compared to pouch cells employing $LiPF_6$-only electrolyte or electrolyte with 0.05 M LiDFP additive, cells

utilizing $LiPF_6$/LiDFP dual-salt electrolyte exhibited significantly reduced TM deposition on graphite. This inhibition prevents persistent solvent decomposition at the anode, thereby suppressing SEI growth and interphasial impedance rise[49,50]. Further, we simulated cathode-derived TM dissolution by introducing Mn^{2+} into the electrolyte, assessing their impact on SEI formed in $LiPF_6$ and $LiPF_6$/LiDFP dual-salt systems. Full-cell cycling performance tests were conducted on reassembled cells employing electrolytes containing 20 mM Mn^{2+} in either 1 M $LiPF_6$ EA/EC or 0.5 M $LiPF_6$ + 0.5 M LiDFP EA/EC, as illustrated in Figures 3h and 3i. The results demonstrate that the interphase derived from the $LiPF_6$/LiDFP dual-salt electrolyte possesses superior resistance to TM ion interference, underscoring its role in stabilizing the CEI/SEI.

LiDFP Forms Thin, Inorganic-Rich CEI

Given LiDFP's interphasial optimization at both electrodes, we characterized interphase structures. Transmission electron microscope (TEM) images (Figures 4a-c) and elemental maps (Figures S9-11) reveal that CEI formed in $LiPF_6$ electrolyte is thick (27.7 nm) and inhomogeneous, indicative of unstable interfacial reactions. Incorporating 0.05 M LiDFP moderately reduced CEI thickness (21.1 nm) and improved compactness. Conversely, $LiPF_6$/LiDFP dual-salt electrolyte formed a thinner (10.8 nm), uniform CEI on cathodes. X-ray photoelectron spectroscopy (XPS) and time of flight secondary ion mass spectrometry (ToF-SIMS) analyses (Figure 4d) confirm all three electrolyte systems yield CEI containing substantial C-O and C=O species on NCM cathodes[10]. The O 1s peak at 529.2 eV corresponds to lithium/TM oxides (M-O), reflecting electrolyte-TM reactions.[51] Dual-salt electrolyte reduced M-O content in CEI, indicating diminished cathode material exposure. LiDFP introduction

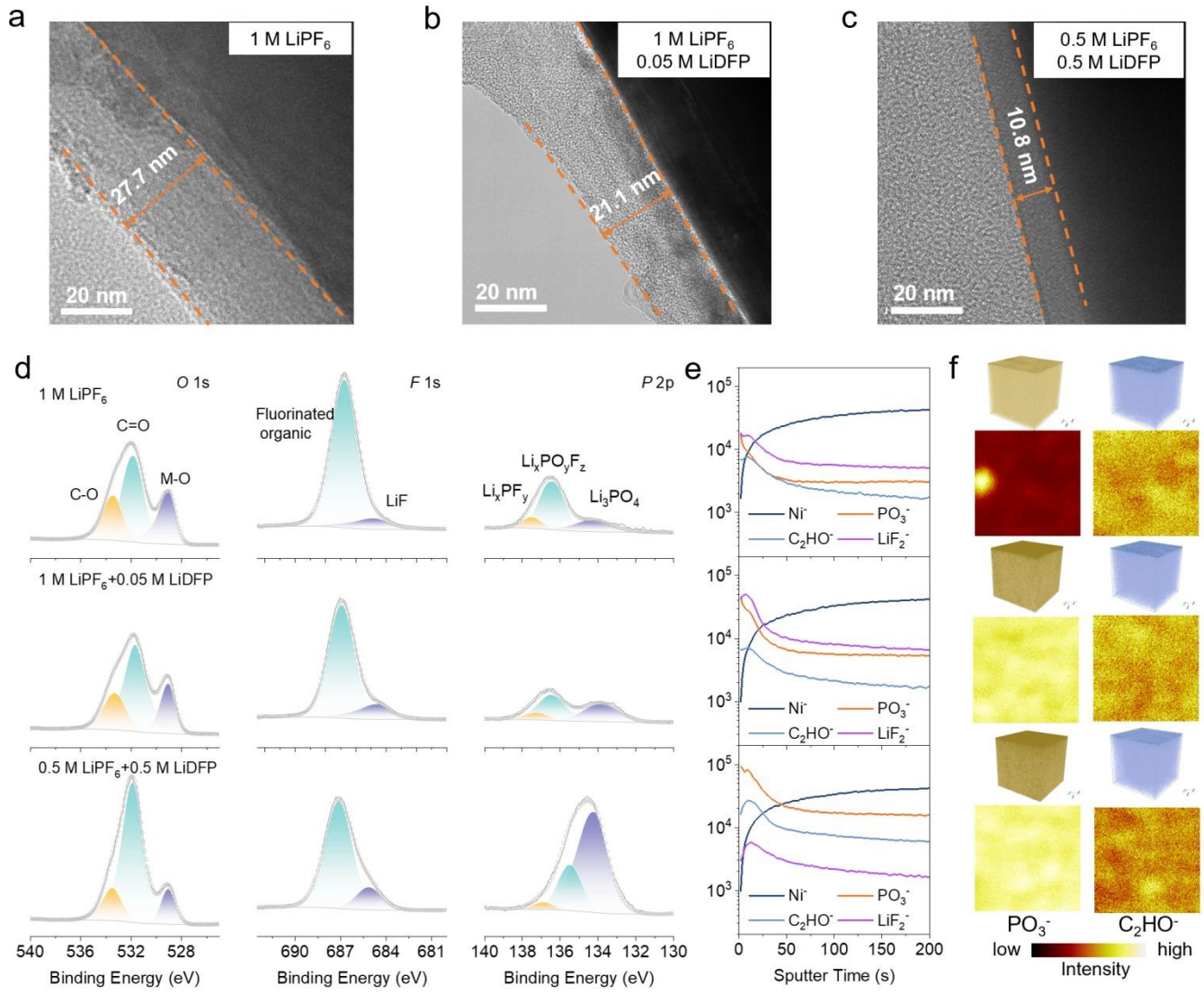

Figure 4. Representative TEM images of cathodes after initial formation in (a) 1 M $LiPF_6$ EA/EC, (b) 1 M $LiPF_6$ + 0.05 M LiDFP EA/EC, and (c) 0.5 M $LiPF_6$ + 0.5 M LiDFP EA/EC electrolytes; (d) Comparative XPS spectra of cathodes cycled in different electrolytes. (e) Depth distribution curves of various secondary ion species of the cathodes with different electrolytes after the initial formation by ToF-SIMS; (f) 3D reconstruction and 2D mapping of interphasial PO_3^- and C_2HO^- secondary ion distributions for NCM613 cathodes.

enhanced CEI compactness, suppressing electrolyte oxidation by delithiated cathodes and TM dissolution. F 1s and P 2p spectra show dual-salt electrolyte significantly increased Li_3PO_4 and LiF content in

CEI. These inorganic components bolster CEI stability, while LiF's high Li^+ mobility and Li_3PO_4's superior ionic conductivity collectively improve interphasial ion transport and reduce organic fluorinated content[52,53]. ToF-SIMS depth profiling (Figure 4e) reveals CEI composition: inorganic species (LiF_2^-, PO_3^-) and organic fragments (C_2HO^-) constitute the interphase.[54] Elevated LiDFP content amplified PO_3^- signals while attenuating C_2HO^- signals, demonstrating LiDFP's efficacy in suppressing solvent decomposition. 3D visualization and 2D distribution of PO_3^- and C_2HO^- ions (Figure 4f) confirm dual-salt electrolyte yields optimized cathode interphase structure post-formation.

LiDFP Promotes Thin, Inorganic-Rich SEI

Beyond CEI, anode SEI critically governs electrochemical performance. We systematically characterized SEI morphology and composition from different electrolytes. TEM results (Figure 5a-c) show that the $LiPF_6$-derived SEI is thicker (23.7 nm), and the addition of 0.05 M LiDFP reduces the SEI thickness but makes it uneven. Dual-salt electrolyte formed a thinner (6.6 nm), homogeneous SEI. XPS and ToF-SIMS analyses elucidated SEI composition (Figure 5d): C 1s spectra feature predominant organic components (C-C, C-O, C=O) in all systems, yet dual-salt electrolyte substantially attenuated these signals. F 1s and P 2p spectra confirm LiDFP promotes inorganic Li_3PO_4 and LiF formation at the anode interphase, with Li_3PO_4 being the primary SEI product from LiDFP decomposition. Depth profiles and 3D/2D distributions of PO_3^- and C_2HO^- ions (Figures 5e-f) illustrate component stratification from surface to bulk. The graphite interphase comprises inorganic (LiF_2^-, PO_3^-) and organic (C_2HO^-) species. Dual-salt electrolyte yields inorganic-rich (LiF_2^-, PO_3^-) SEI with reduced organic content, favoring robust interphasial kinetics. Hence, LiDFP as a mixed main salt significantly enhances battery performance by forming dense and stable CEI and SEI rich in Li_3PO_4 and LiF inorganic components at both electrode interphases. These interphasial analyses indicate that the high concentration and weak dissociation of LiDFP in the electrolyte facilitate the formation of

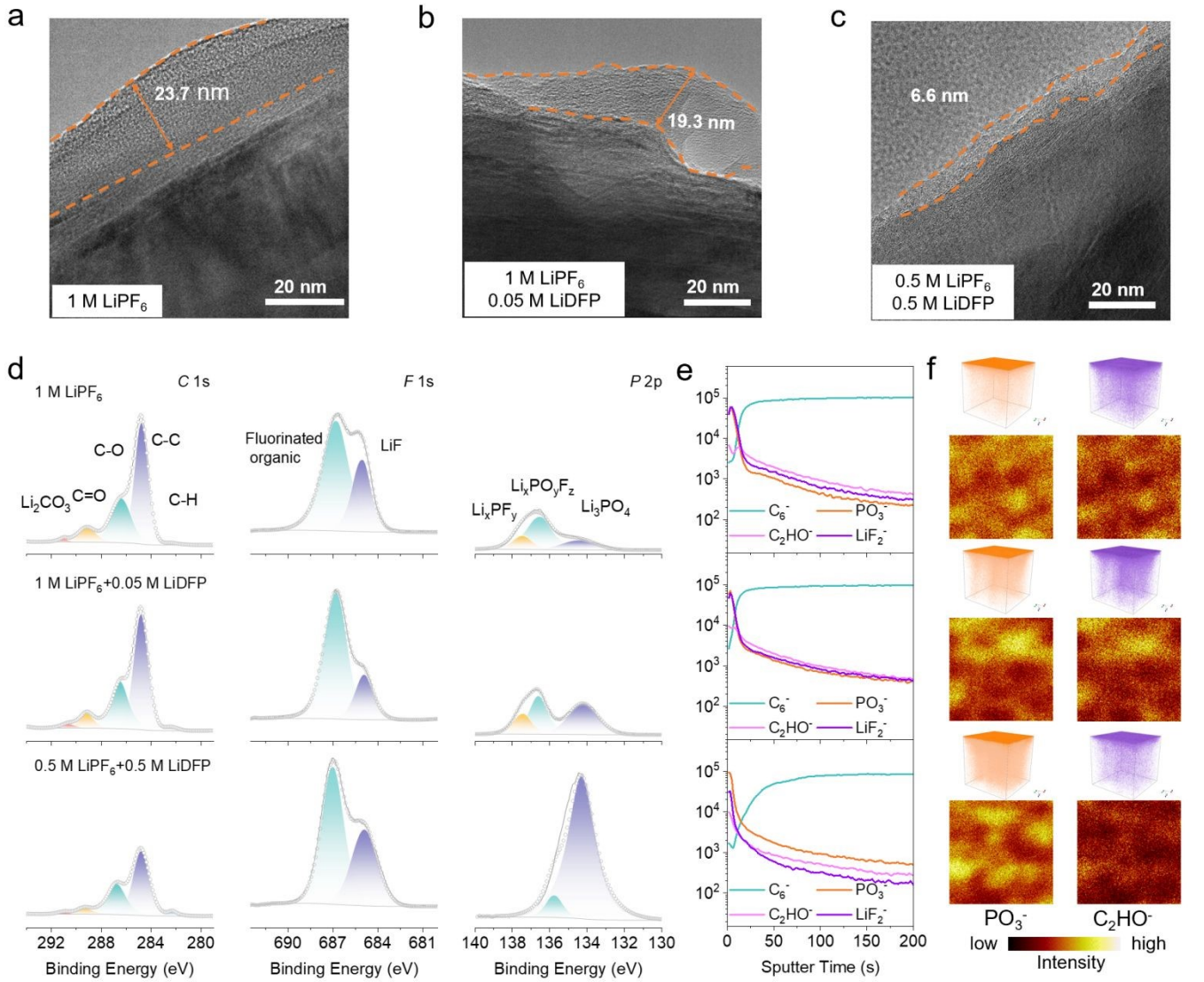

Figure 5. Representative TEM images of anodes after initial formation in (a) 1 M $LiPF_6$ EA/EC, (b) 1 M $LiPF_6$ + 0.05 M LiDFP EA/EC, and (c) 0.5 M $LiPF_6$ + 0.5 M LiDFP EA/EC electrolytes; (d) Comparative XPS spectra of cathodes cycled in different electrolytes. (e) Depth distribution curves of various secondary ion species of the anodes with different electrolytes after the initial formation by ToF-SIMS; (f) 3D reconstruction and 2D mapping of interphasial PO_3^- and C_2HO^- secondary ion distributions for graphite cathodes.

phosphate-rich and organic-lean CEI/SEI, which significantly enhances interphase stability and prolongs battery life.

Conclusions

We employed a dual-salt electrolyte (0.5 M LiDFP/0.5 M $LiPF_6$) in an EA/EC co-solvent, which rendered a stable wide-temperature lithium-ion battery operation. The weak dissociation of LiDFP predominantly forms CIPs and AGGs, substantially increasing the $PO_2F_2^-$ anion coordination number within the primary solvation shell surrounding Li^+. This regulated solvation structure drives preferential anion decomposition at electrode surfaces, generating thin, dense, inorganic-rich (Li_3PO_4 and LiF) CEI and SEI layers. Consequently, 5 Ah NCM613||graphite pouch cells exhibit >80% capacity retention after 200 cycles at 60°C and deliver 57% reversible capacity at -40°C. This work demonstrates an industrially viable electrolyte design strategy for wide-temperature batteries through precise control of lithium salt dissociation and solvation dynamics.

Experimental

Electrolytes and electrodes preparation.

The raw materials for the electrolytes are purchased from Guangzhou Tinci Materials Technology Co., Ltd. at the battery-grade specification. EA/EC (7:3 v/v) solvent system was employed with varying $LiPF_6$/LiDFP ratios (1 M $LiPF_6$, 1 M $LiPF_6$ + 0.05 M LiDFP, and 0.5 M $LiPF_6$ + 0.5 M LiDFP).

The NCM613 cathode contained 96.5 wt.% NCM613 material, super P as the conductive agent and PVDF as the binder. The graphite anode contained 97 wt.% artificial graphite and SBR as the binder. The size of these pouch cells is 8.3 mm * 66 mm * 79 mm, the designed capacity is about 4.8 Ah, and the charging/discharging voltage range is 3.0~4.28 V. The NCM613||graphite pouch cells were assembled in the pouch-cell production line and each pouch cell was filled with 20 g of the electrolyte. The entirety of the electrode and pouch cell preparation procedure was scrupulously conducted within a dry room environment, assured by maintaining a dew point below -40°C to prevent any moisture-induced compromises during the production process. The half cells were meticulously assembled into 2032-type coin cells, incorporating a polypropylene (PP) separator saturated with 50 µL of electrolyte. The intricate assembly process took place within the inert confines of an argon-filled glovebox, where both water and oxygen levels were stringently controlled to remain below 0.1 ppm.

Electrochemical measurements.

Linear sweep voltammetry (LSV) was carried out to evaluate the redox potential of the electrolytes. The positive scan was conducted from open circuit potential to 6 V (vs. Li^+/Li) with Pt as working electrode and Li metal as Counter electrode & reference electrode, and the negative scan was conducted from open circuit potential to 0.01 V. The scanning rate is 1 mV/s. The cycle performance test at 25°C, 45°C and 60°C were performed with Neware battery test system. The cycling protocol is set up as follow: Firstly, charge the cell to 4.28 V at 1C, and then charge at a constant voltage of 4.28 V until the current reaches 0.05C followed by 5 min rest. Secondly, discharge to 3.0 V at 1C followed by 5 min rest. Repeat the above steps until the discharge capacity retention reaches 80%. It should be noted that a cycle for 0.2C charging-discharging was conducted every 100 cycles.

Material Characterization.

Raman spectra were acquired on HORIBA HR Evolution featuring a 532 nm laser source for excitation. TEM images were taken using a High-Resolution Transmission Electron Microscope (Talos F200X). ICP-AES tests were conducted on PE ICP 7000DV. XPS measurements were performed on the depth-profiling X-ray photoelectron spectroscopy (ESCALAB 250Xi). A specially designed airtight apparatus was used to transfer the electrodes into the XPS system without exposure to air. TOF-SIMS was performed on a ToF-SIMS5-100 instrument at Vacuum interconnected nanotech workstation SINANO, CAS. For the SEI study, the electrodes after cycling were disassembled in a glove box and rinsed several times with DMC to remove residual electrolytes.

Calculation methods.

Molecular dynamics (MD) simulations for all electrolyte systems were performed with GROMACS simulation package, version 2019.3 using OPLS-AA force fields (Optimized Potentials for Liquid Simulations All Atom) while the bonded and non-bonded parameters for solvent molecules were obtained from LigParGen, a publicly accessible web server[55,56]. The partial atomic charges for solvents were calculated by Gaussian 16 program in PBE0/def2TZVP level and following Hirshfeld population analysis. CM5 charges were mapped with Multiwfn code and scaled by a factor of 1.2[57,58]. For each simulation system, in sum of 1500 molecules including solvent and salt components were initially packed randomly in a cubic box with primary size of 65 Å x 65 Å x 65 Å using PACKMOL[59]. For facilitating the equilibration of the system, annealing process was conducted with NPT ensemble before production simulation, in which the system was heated to 400 K and kept for 1 ns, then cool down to 298 K within a time interval of 1 ns and kept at 298 K for another 1 ns. After that, production simulation running for 5 ns were also performed in the NPT ensemble, under Nose–Hoover thermostats and Parrinello–Rahman barostat to maintain a pressure of 1 atm and a temperature of 298 K. Further results were analyzed from the trajectory data by GROMACS tool-suites and visual molecular dynamics (VMD) software[60]. The relevant quantum chemical (QC) calculations of Figure S2 were conducted with Gaussian 16 (Revision C.01) using density functional theory (DFT) at PBE0/ma-TZVP level.

Author contributions

Shaoyun Zhou, Zetai Xu and Chaonan Wang equally contributed to this work.

Conflicts of interest

There are no conflicts to declare.

Data availability

The data supporting the findings of this study are available from the corresponding author upon reasonable request. Supplementary information (SI) is available. See DOI:

Acknowledgements

We appreciate funding support from the National Natural Science Foundation of China (22125902, 22109150, and 22279126), the Anhui Science Fund for Distinguished Young Scholars (2408085J009), USTC Tang Scholar, the Fundamental Research Funds for the Central Universities (WK2490000002), as well as the Major Industrial Innovation Program of Anhui Province (BJ9980008003). We thank Nano-X (SINANO, CAS) for assistance with characterization. The simulations were performed on the robotic AI-Scientist platform of Chinese Academy of Sciences.

References

1 M. Li, J. Lu, Z. Chen, K. Amine, *Adv. Mater.*, 2018, **30**, 1800561.
2 M. Winter, B. Barnett, K. Xu, *Chem. Rev.*, 2018, **118**(23), 11433-11456.
3 B. Dunn, H. Kamath, J. M. Tarascon, *Science*, 2011, **334**(6058), 928-935.
4 J. Xu, V. Koverga, A. Phan, A. min Li, N. Zhang, M. Baek, C. Jayawardana, B. L. Lucht, A. T. Ngo, C. Wang, *Adv. Mater.,* 2024, **36**, 2306462.
5 H. Zhang, Y. Zhao, X. Li, H. Wang, L. Wang, Y. Song, F. Qiao, J. Wang, J. Xu, *Adv. Sci.*, 2025, **12**(32), e03151.
6 X. Yang, P. Li, C. Guo, W. Yang, N. Zhou, X. Huang, Y. Yang, *J. Power Sources*, 2024, **624**, 235563.
7 J. Wang, W. Huang, A. Pei, Y. Li, F. Shi, X. Yu, Y. Cui, *Nat. Energy*, 2019, **4** (8), 664-670.
8 X. Yang, J. Chen, Q. Zheng, W. Tu, L. Xing, Y. Liao, M. Xu, Q. Huang, G. Cao, W. Li, *J. Mater. Chem. A*, 2018, **6** (33), 16149-16163.
9 J. Hou, M. Yang, D. Wang, J. Zhang, *Adv. Energy Mater.*, 2020, **10** (18), 1904152.
10 W. Zhao, B. Zheng, H. Liu, F. Ren, J. Zhu, G. Zheng, S. Chen, R. Liu, X. Yang, Y. Yang, *Nano Energy*, 2019, **63**, 103815.
11 W. Zhao, G. Zheng, M. Lin, W. Zhao, D. Li, X. Guan, Y. Ji, G Ortiz, Y. Yang, *J. Power Sources*, 2018, **380**, 149-157.
12 Y. Yin, X. Dong, *Interd. Mater.*, 2023, **2** (4), 569-588.
13 N. Zhang, T. Deng, S. Zhang, C. Wang, L. Chen, C. Wang, X. Fan, *Adv. Mater.*, 2022, **34** (15), 2107899.
14 N. Piao, X. Gao, H. Yang, Z. Guo, G. Hu, H. Cheng, F. Li, *Etransportation*, 2022, **11**, 100145.
15 C. Villevieille, *Nat. Nanotechnol.*, 2025, **20** (1), 2-5
16 J. Popovic, *Nat. Commun.*, 2021, **12** (1), 6240.
17 Y. Liao, H. Zhang, Y. Peng, Y. Hu, J. Liang, Z. Gong, Y. Wei, Y. Yang, *Adv. Energy Mater.*, 2024, **14** (18), 2304295.
18 S. Hu, H. Zhao, Y. Qian, S. Xiang, G. Zhang, W. Huang, G. Luo, J. Wang, Y. Deng, C. Wang, *J. Energy Storage*, 2023, **57**, 106266.
19 X. Fan, C. Wang, *Chem. Soc. Rev.*, 2021, **50** (18), 10486-10566.
20 K. Xu, *Chem. Rev.*, 2014, **114** (23), 11503-11618.
21 Z. Liu, J. Chai, G. Xu, Q. Wang, G. Cui, Coordin. *Chem. Rev.*, 2015, **292**, 56-73.
22 X. Min, C. Han, S. Zhang, J. Ma, N. Hu, J. Li, X. Du, B. Xie, H. Lin, C. Kuo, C. Chen, Z. Hu, L. Qiao, Z. Cui, G. Xu, G. Cui, *Angew. Chem. Int. Edit.*, 2023, **62** (34), e202302664.
23 D. Abraham, M. Furczon, S. Kang, D. Dees, A. Jansen, *J. Power Sources*, 2008, **180** (1), 612-620.
24 J. Eom, I. Jung, J. Lee, *J. Power Sources*, 2011, **196** (22), 9810-9814.
25 T. Hou, G. Yang, N. Rajput, J. Self, S. Park, J. Nanda, K. Persson, *Nano Energy*, 2019, **64**, 103881.
26 M. Kim, H. Moon, S. Kim, Y. Cho, T. Lee, S. Park, H. Kim, Y. Kwon, S. Hong, N. Choi, *Chem. Eng. J.*, 2025, **511**, 162079.
27 B. Nan, L. Chen, N. Rodrigo, O. Borodin, N. Piao, J. Xia, T. Pollard, S. Hou, J. Zhang, X. Ji, J. Xu, X. Zhang, L. Ma, X. He, S. Liu, H. Wan, E. Hu, W. Zhang, K. Xu, X. Yang, B. Lucht, C. Wang, *Angew. Chem. Int. Edit.*, 2022, **61** (35), e202205967.
28 P. Zhou,W. Hou, Y. Xia, Y. Ou, H. Zhou, W. Zhang, Y. Lu, X. Song, F. Liu, Q. Cao,H. Liu, S. Yan, K. Liu, *ACS Nano*, 2023, **17** (17), 17169-17179.
29 H. Li, C. Yan, S. Wang, *EcoEnergy*, 2025;**3**(2):387-421.
30 Y. Jie, Dr. X. Liu, Z. Lei, S. Wang, Y. Chen, F. Huang, R. Cao, G. Zhang, S. Jiao, *Angew. Chem. Int. Edit.*, 2020, **59** (9), 3505-3510.
31 H. Zheng, H. Xiang, F. Jiang, Y. Liu, Y. Sun, X. Liang, Y. Feng, Y. Yu, *Adv. Energy Mater.*, 2020, **10** (30), 2001440.
32 S. Tan, Z. Shadike, J. Li, X. Wang, Y. Yang, R. Lin, A. Cresce, J. Hu, A. Hunt, I. Waluyo, L. Ma, F. Monaco, P. Cloetens, J. Xiao, Y. Liu, X. Yang, K. Xu, E. Hu, *Nat. Energy*, 2022, **7**(6): 484-494.
33 G. Yang, J. Shi, C. Shen, S Wang, L. Xia, H. Hu, H. Luo, Y. Xia, Z. Liu, *RSC Adv.*, 2017, **7**(42): 26052-26059.
34 Q. Zheng, G. Li, X. Zheng, L. Xing, K. Xu , W. Li, *Energy & Environ. Mater.*, 2022, **5**(3): 906-911.
35 M. Liu, Z. Zeng, C. Gu,F. Ma, Y. Wu, Q. Wu, X. Yang, X. Chen, S. Cheng, J. Xie, *ACS Energy Lett.*, 2023, **9**(1): 136-144.
36 N Y. Yamada, Y. Takazawa, K. Miyazaki, T. Abe, *J. Phys. Chem. C.*, 2010, **114** (26), 11680-11685.
37 H. Kim, K. Lim, G. Yoon, J. Park, K. Ku, H. Lim, Y. Sung, K. Kang, *Adv. Energy Mater.*, 2017, **7**(19), 1700418.
38 K. Yoshida, M. Nakamura, Y. Kazue, N. Tachikawa, S. Tsuzuki, S. Seki, K. Dokko, M, Watanabe, *J. Am Chem Soc.*, 2011, **133**(33): 13121-13129.
39 Z. Li,1 N. Yao, L. Yu, Y. Yao, C. Jin, Y. Yang, Y. Xiao, X. Yue, W. Cai, L. Xu, P. Wu, C. Yan, and Q. Zhang, *Matter*, 2023, **6**(7): 2274-2292.
40 Y. Wu, Q. Hu, H. Liang, A. Wang, H. Xu, L. Wang, X. He, *Adv. Energy Mater.*, 2023, **13**(22), 2300259.
41 A. Wang, L. Wang, H. Liang, Y. Song, Y. He, Y. Wu, D. Ren, B. Zhang, X. He, *Adv. Funct. Mater.*, 2023, **33**(8), 2211958.
42 Y. Chen, Q. He, Y. Zhao, W. Zhou, P. Xiao, P. Gao, N. Tavajohi, J. Tu, B. Li, X. He, L. Xing, X. Fan, J. Liu. *Nat. Commun.*, 2023, **14**, 8326.
43 Y. Chen, A. Wang, Y. Zhao, W. Wang, R. Dominko, P. Xiao, P. Gao, Y. Duan, B. Li, X. He, J. Liu, 2026, **13**(3), nwaf543.
44 T. Pham, B. Faheem, K. Kwak, K. Lee, Batteries & Supercaps, 2025, **8**, e202500163.
45 X. Zheng, Z. Cao, W. Luo, S. Weng, X. Zhang, D. Wang, Z. Zhu, H. Du, X. Wang, L. Qie, H. Zheng, Y. Huang, *Adv. Mater.*, 2023, **35**, 2210115.

View Article Online
DOI: 10.1039/D6EB00057F

46 Y. Zou, Z. Ma, G. Liu, Q. Li, D. Yin, X. Shi, Z. Cao, Z. Tian, H. Kim, Y. Guo, C. Sun, L. Cavallo, L. Wang, H. N. Alshareef, Y.-K. Sun, J. Ming, *Angew. Chem. Int. Ed.*, 2023, **62**, e202216189.
47 Z. Li, Y.-X. Yao, M. Zheng, S. Sun, Y. Yang, Y. Xiao, L. Xu, C.-B. Jin, X.-Y. Yue, T. Song, P. Wu, C. Yan, Q. Zhang, *Angew. Chem. Int. Ed.*, 2025, **64**, e202409409.
48 W. Yang, W. Chen, H. Zou, J. Lai, X. Zeng, Y. Zhang, X. Zeng, K. Ding, S. Zhang, L. Ma, Z. Li, Q. Zheng, *Angew. Chem. Int. Ed.*, 2025, **64**, e202424353.
49 R. Thangavel, V. Ahilan, M. Moorthy, W. Yoon, S. Shanmugam, Y. Lee, *J. Power Sources*, 2021, **484**, 229143.
50 L. Britala, M. Marinaro, G. Kucinskis, *Adv. Energy Mater.*, 2024, **14**(19), 2303468.
51 Y. Chen, W. Zhao, Q. Zhang, G. Yang, J. Zheng, W. Tang, Q. Xu, C. Lai, J. Yang, C. Peng, *Adv. Funct. Mater.*, 2020, **30**(19), 2000396.
52 J. Chen, X. Fan, Q. Li, H. Yang, M. Khoshi, Y. Xu, S. Hwang, L. Chen, X. Ji, C. Yang, H. He, C. Wang, E. Garfunkel, D. Su, O. Borodin, C. Wang, *Nat. Energy,* 2020, **5**, 386–397.
53 Y. Chen, Y. Zhao, A. Wang, D. Zhang, B. Li, X. He, X. Fan, J. Liu, *Energy Environ. Sci.*, 2024, **17**, 6113-6126.
54 Y. Xie, Y. Huang, H. Chen, W. Lin, T. Wu, Y. Wang, S. Liu, M. Sun, H. Huang, P. Dai, Y. Ding, D. Wu, C. Ouyang, Y. Hong, X. Li, C. Liu, S. Liao, L. Huang, S. Sun, *Adv. Funct. Mater.*, 2024, **34**(21), 2310867.
55 L. S. Dodda, I. C. De Vaca, J. Tirado-Rives, LigParGen web server, *J. Nucleic Acids Res.*, 2017, **45**(W1), W331-W336.
56 S. V. Sambasivarao, O. Acevedo, *J. Chem. Theory Comput*., 2009, **5**(4), 1038-1050.
57 L. S. Dodda, J. Z. Vilseck, J. Tirado-Rives, *J. Phys. Chem. B*, 2017, **121**(15), 3864-3870.
58 T. Lu, F. Chen, W. Multiwfn, *J. Comput. Chem.*, 2012, **33**(5), 580-592.
59 L. Martínez, R. Andrade, E. G. Birgin, *J. Comput. Chem.*, 2009, **30**(13), 2157-2164.
60 W. Humphrey, A. Dalke, K. Schulten, *J. Mol. Graph. Model.*, 1996, **14**(1), 33-38.

View Article Online
DOI: 10.1039/D6EB00057F

Data availability

The data supporting this article have been included as part of the Supplementary Information.